Electronic Supplementary Information (ESI)

Solar-driven photocatalytic removal of NO over the concrete paving Eco-block containing black TiO_2

Pengyu Dong,*[a] Cunxia Wang,[ab] Junjian Tan,[ab] Yan Wang,[a] Xinguo Xi*[c] and Jinlong Zhang*[d]

[a] *Key Laboratory for Advanced Technology in Environmental Protection of Jiangsu Province, Yancheng Institute of Technology, Yancheng 224051, P. R. China.*

[b] *School of Mechanical Engineering, Yancheng Institute of Technology, Yancheng 224051, P. R. China.*

[c] *Key Laboratory for Ecological-Environment Materials of Jiangsu Province, School of Materials Science and Engineering, Yancheng Institute of Technology, Yancheng 224051, PR China.*

[d] *Key Laboratory for Advanced Materials and Institute of Fine Chemicals, School of Chemistry & Molecular Engineering, Shanghai Engineering Research Center for Multi-media Environmental Catalysis and Resource Utilization, East China University of Science and Technology, 130 Meilong Road, Shanghai 200237, China.*

*Corresponding authors.

**Email for P.D: dongpy11@gmail.com; *Email for X.X: xxg@ycit.cn; *Email for J.Z: jlzhang@ecust.edu.cn.*

1. Additional details of the preparation of black TiO_2 photocatalyst

Black TiO_2 (B-TiO_2) photocatalyst was prepared according to the References with some modifications.[1] The preparation details were described as follows: At room temperature (25 °C) and 50% relative humidity, 2.0 g of white TiO_2 (W-TiO_2) nanoparticle powder (P25) was mixed with 1.25 g of $NaBH_4$ and the mixture was ground for 30 min thoroughly. Then the mixture was transferred into a porcelain boat, and placed in a tubular furnace, heated from room temperature to 350 °C under an Ar atmosphere at a heating rate of 10 °C/min, and then held at the designated temperature for 60 min. After naturally cooling down to room temperature, the obtained powder was washed with deionized water and ethanol 5 times to remove unreacted $NaBH_4$, respectively, and dried in an oven at 70 °C overnight to obtain B-TiO_2.

2. Preparation of the suspension containing photocatalyst

To obtain the suspension, various amounts of B-TiO_2 (e.g. 50, 100, 200, and 300 mg) and the binder (i.e. water-glass (Na_2O•nSiO_2, n=2)) were added to 10 mL deionized water, respectively, and stirred for 2 h, and then treated by ultrasound-assisted dispersion for 30 min to form various suspension. The corresponding concentration of B-TiO_2 in suspension was 5, 10, 20, and 30 mg/mL, respectively. For comparison purposes, the suspension of W-TiO_2 with a concentration of 20 mg/mL, and the suspension of B-TiO_2 and W-TiO_2 (20 mg/mL) without the binder were prepared by a similar method as described above.

3. Mechanical testing of concrete paving Eco-block

The test details and calculation formula of abrasion resistance of as-prepared concrete paving Eco-blocks are described as follows. After starting up, it ground for 30 revolutions, and then the initial grinding depth was measured and recorded as P_0. When the rotor turns per 1000 revolutions, the

grinding depth of the groove was measured once time. When the number of revolutions of the grinding head reaches 4000 rpm, the test will be terminated. The grinding depth was measured by a vernier caliper, and the average value (P_f) was taken as the grinding depth in all four directions, which is accurate at 0.01 mm. The final grinding depth was estimated according to the following equation (Eq. (1)):

$$P = P_f - P_0 \tag{1}$$

The grinding depth after a certain rotating revolution was obtained. Then, the abrasion resistance of concrete paving Eco-block samples can be calculated by using the following equation (Eq. (2)).

$$I_S = \frac{\sqrt{R}}{P} \tag{2}$$

where I_s is the abrasion resistance ($kr^{1/2}$ / mm);

R is the rotating revolutions of the grinding wheel, kr;

P is the grinding depth, mm.

4. CFD modeling details

In the discussion of the traveling vehicle pollutant emission problem, we simplified the problem by considering the pollution source term that a traveling vehicle pollutant emission rate. During the vehicle driving process, the flow of traffic from the macroscopic view is similar to the flow of water as a whole due to the speed of the rear vehicle and vehicle distance constrained by the front vehicle, which meets the characteristics of the fluid. Comprehensive consideration of the impact factors of the NO emission rate of a vehicle, such as the working condition of the vehicle, altitude, the slope of the driving road, the type of vehicle, the size of traffic flow, driving speed, etc., the NO emission rate of a single driving vehicle could be expressed as follows.

$$Q_{NO} = \frac{q_{NO} \cdot f_a \cdot f_d \cdot f_h \cdot f_{iv} \cdot v \cdot f_m}{3.6 \times 10^3 \, L} \quad (4)$$

where Q_{NO} represents the NO emission rate of individual vehicle ($m^3\ s^{-1}$), q_{NO} is the baseline emission of NO (m^3 veh.$^{-1}$ km^{-1}), f_a represents the coefficient of vehicle condition considering NO (always 1.0), f_d is the vehicle density coefficient (3.0 in the normal driving conditions and 6.0 in the case of traffic congestion), f_h is the altitude factor (1.0 in Yancheng), f_{iv} represents the slope longitudinal coefficient (1.0 for smooth traffic flow and 0.8 for stagnant traffic), v represents the vehicle travel speed (assuming 60 km h^{-1} for normal operation and 10 km h^{-1} for traffic congestion), and f_m represents the vehicle model coefficient (1.0 for a car).

5. Additional Figures and Tables

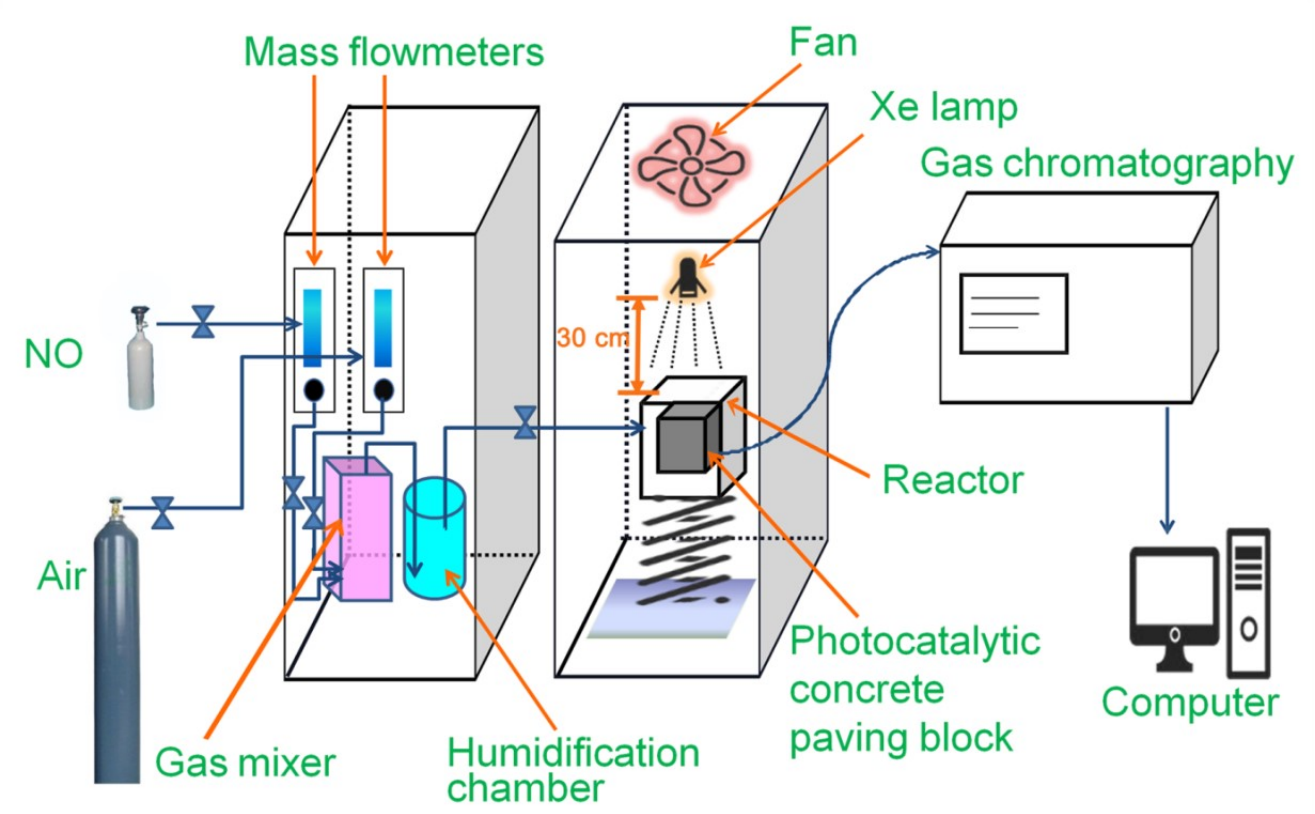

Scheme S1 The diagrams of equipment for photocatalytic NO removal.

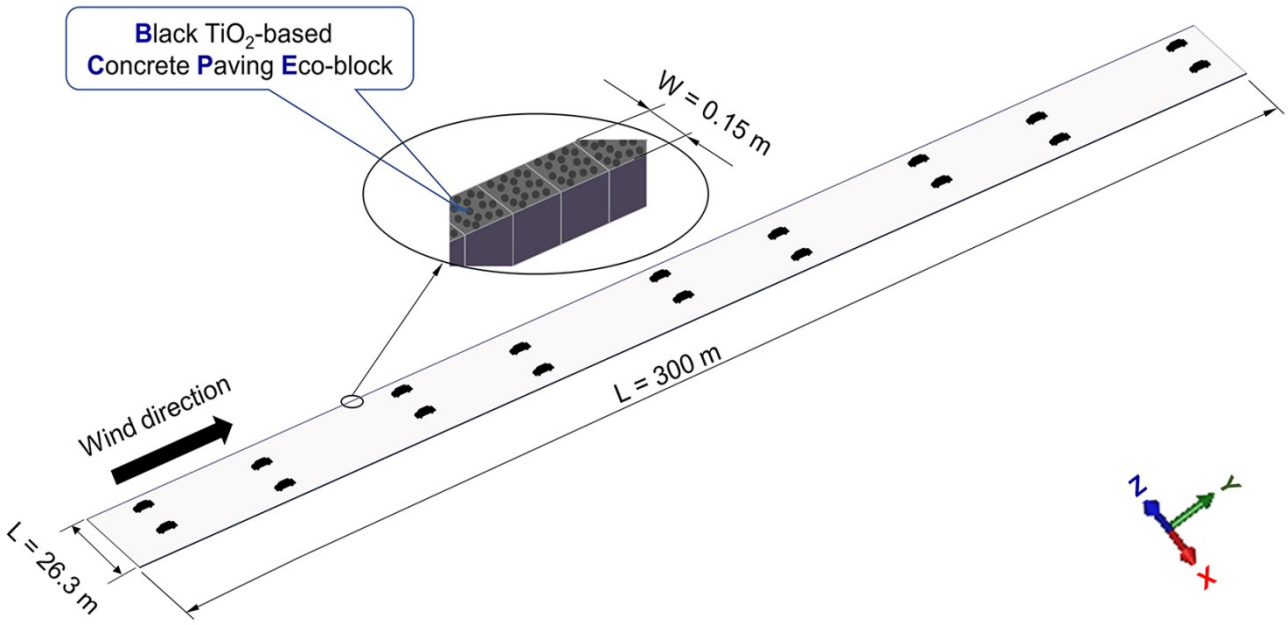

Scheme S2 The CFD modeling for simulating the wind flow and traffic-related NO concentration in a realistic urban street coated with black TiO_2-based photocatalytic concrete paving Eco-blocks on the two sides of the street considering the effects of wind speed and traffic environment (taking the vehicle speed of 60 km h^{-1} as an example).

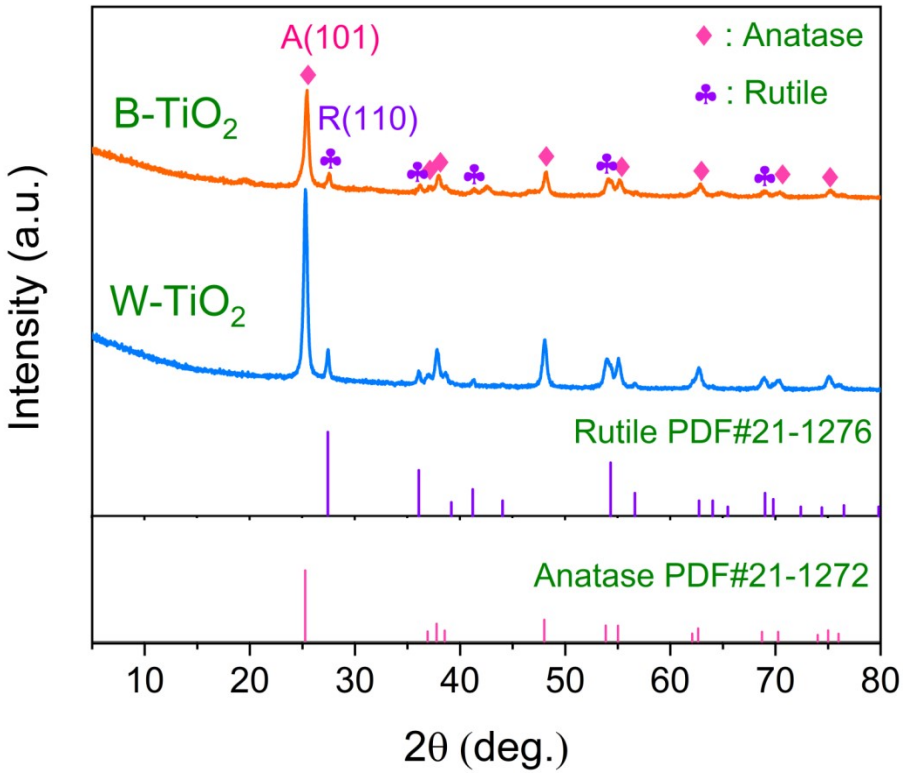

Fig. S1 XRD patterns of W-TiO_2 and B-TiO_2.

Both W-TiO_2 and B-TiO_2 show anatase and rutile phases (Fig. S1). Moreover, the integrated intensities of the diffraction peaks in the XRD patterns could be used to estimate the contents of these two phases [2], as depicted in Eq. (5).

$$W_R = \frac{A_R}{0.884A_A + A_R} \quad (5)$$

where A_A and A_R stand for the anatase (101) peak's and rutile (110) peak's integrated intensities, respectively. Herein, the calculated weight fraction of rutile (W_R) in B-TiO_2 is 19.4 wt%, which means that the weight fraction of anatase (W_A) is 80.6 wt%. For comparison, the calculated W_R and W_A in W-TiO_2 are 19.6 wt% and 80.4 wt%, respectively.

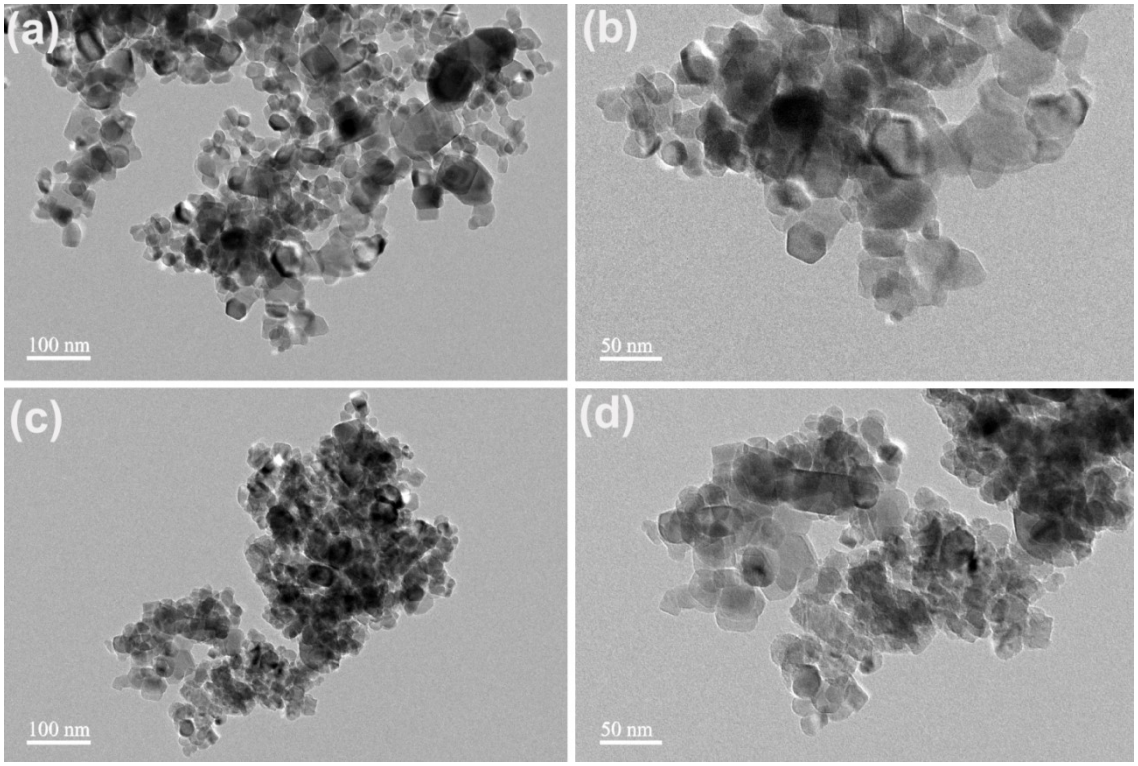

Fig. S2 TEM images of (a, b) W-TiO_2 (P25) and (c, d) B-TiO_2.

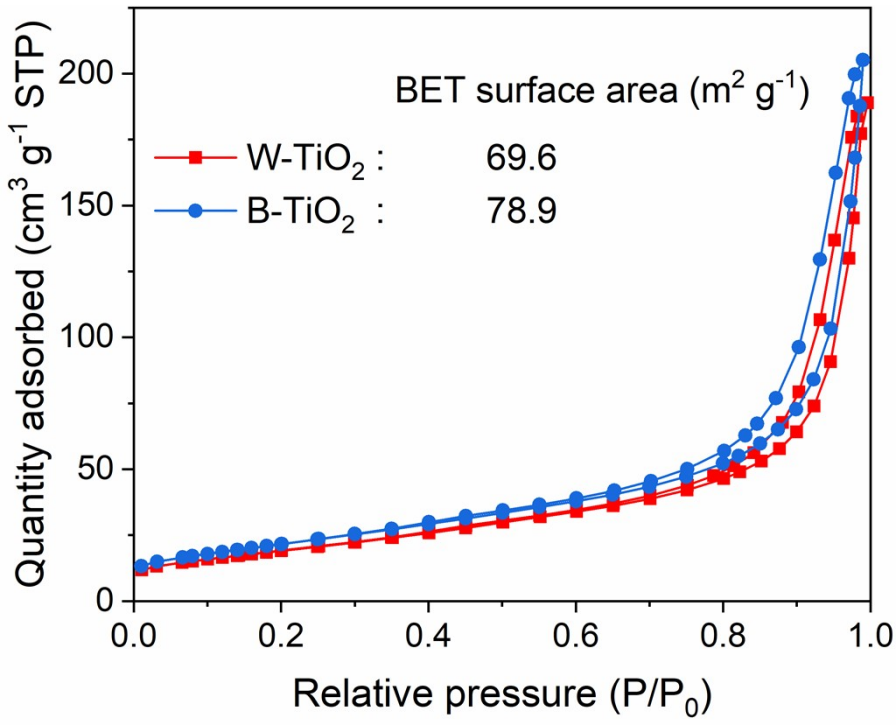

Fig. S3 N_2 adsorption and desorption isotherm of W-TiO_2 and B-TiO_2.

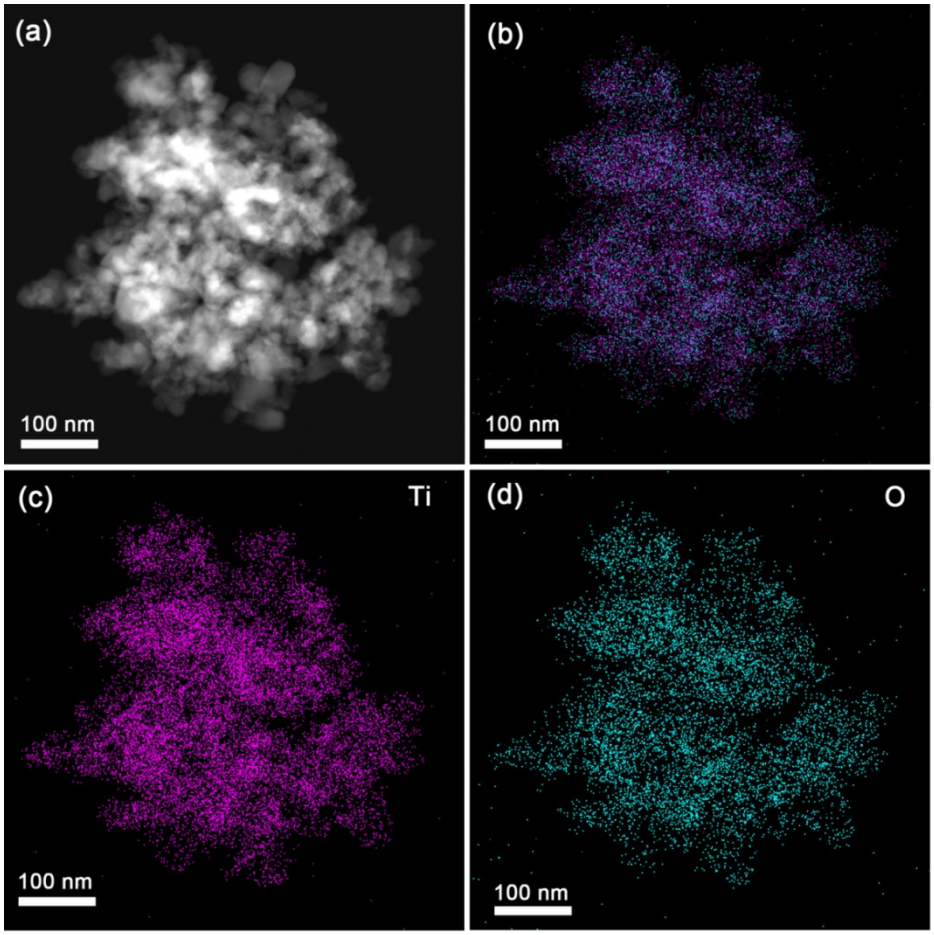

Fig. S4 (a) HAADF-STEM image and (b-d) the corresponding EDX elemental mapping images for the sample of B-TiO_2.

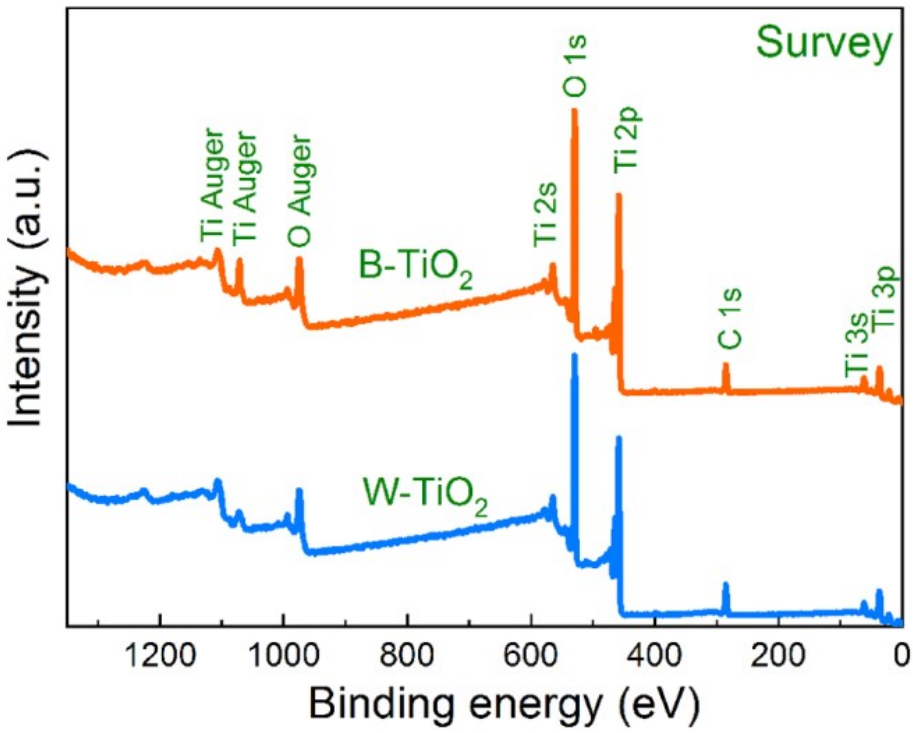

Fig. S5 XPS survey spectra of the as-prepared B-TiO_2 and W-TiO_2.

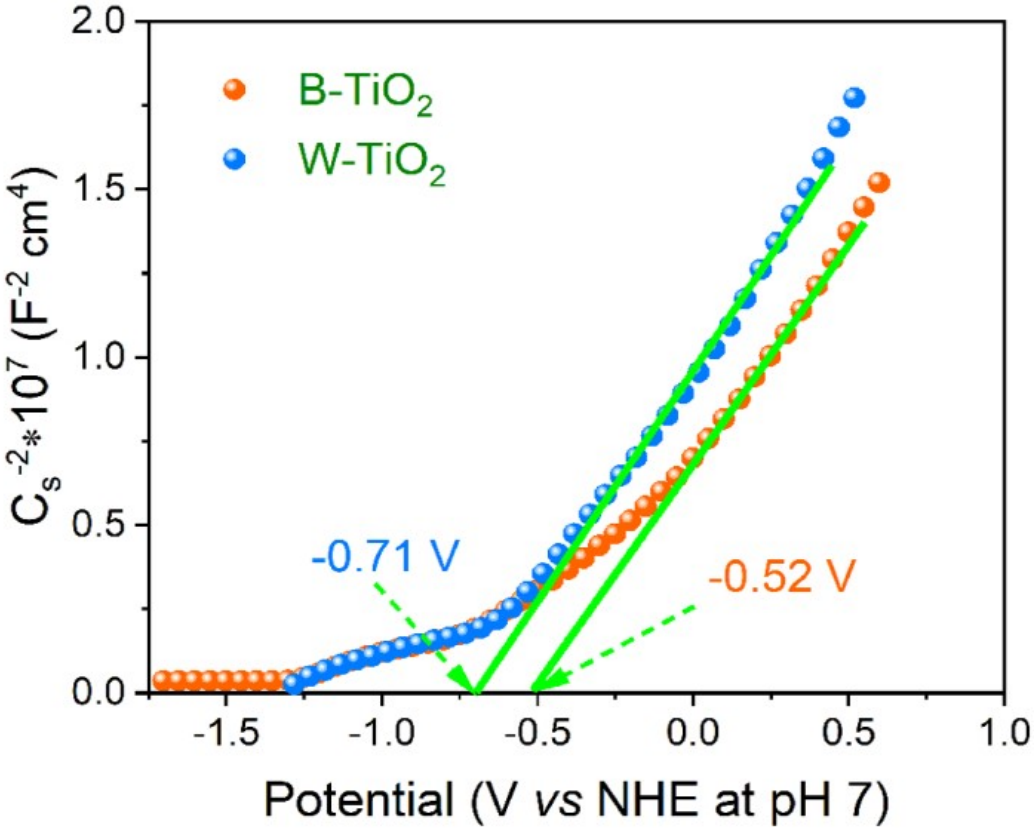

Fig. S6 Mott−Schottky plots of the as-prepared B-TiO_2 and W-TiO_2 measured with Ag/AgCl as the reference electrode in the dark.

The Mott-Schottky plots of the as-prepared B-TiO_2 and W-TiO_2 were measured to further identify the energy band position. As shown in Fig. S4, the positive sloped linear region indicates the feature of a characteristic n-type semiconductor and the *x*-intercept reflects the flat band potentials (E_{fb}) of B-TiO_2 and W-TiO_2, which are −0.52 and −0.71 V *vs.* NHE at pH 7, respectively. Therefore, the E_{fb} of B-TiO_2 and W-TiO_2 are close to their E_{CB} positions from UPS results as displayed in Fig. 1i.

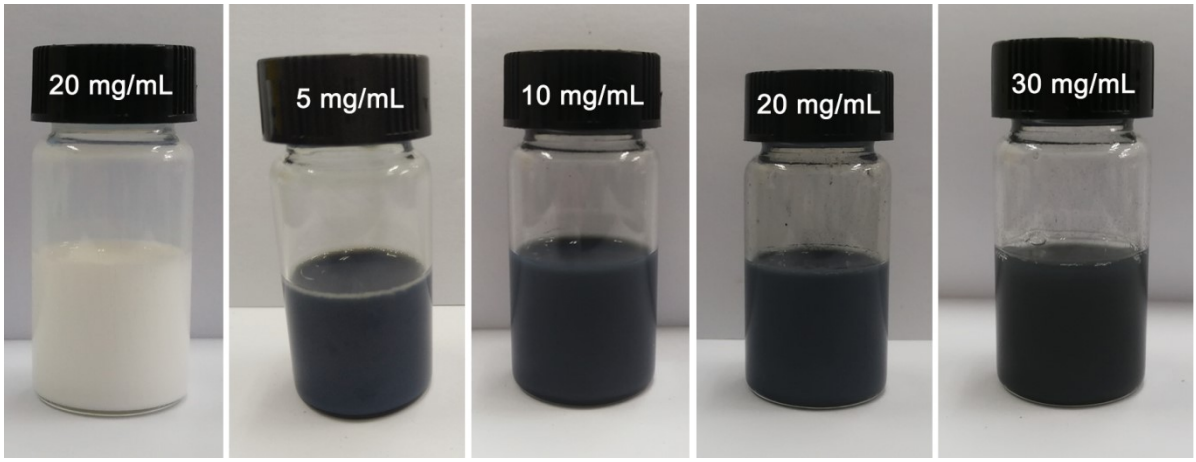

Fig. S7 Digital pictures of the suspension containing W-TiO_2 and B-TiO_2 with various concentrations after standing for 1 day.

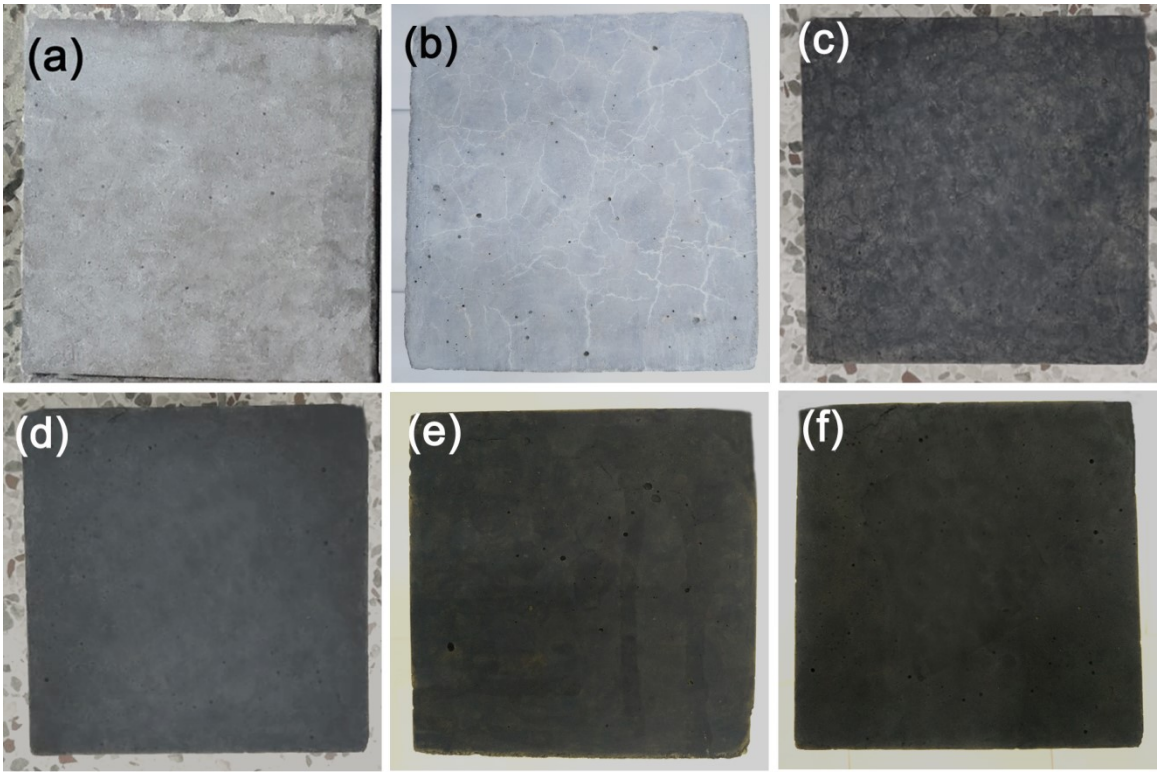

Fig. S8 Photographs of surface layers of (a) blank control, (b) WCPE-20, (c) BCPE-5, (d) BCPE-10, (e) BCPE-20, and (f) BCPE-30.

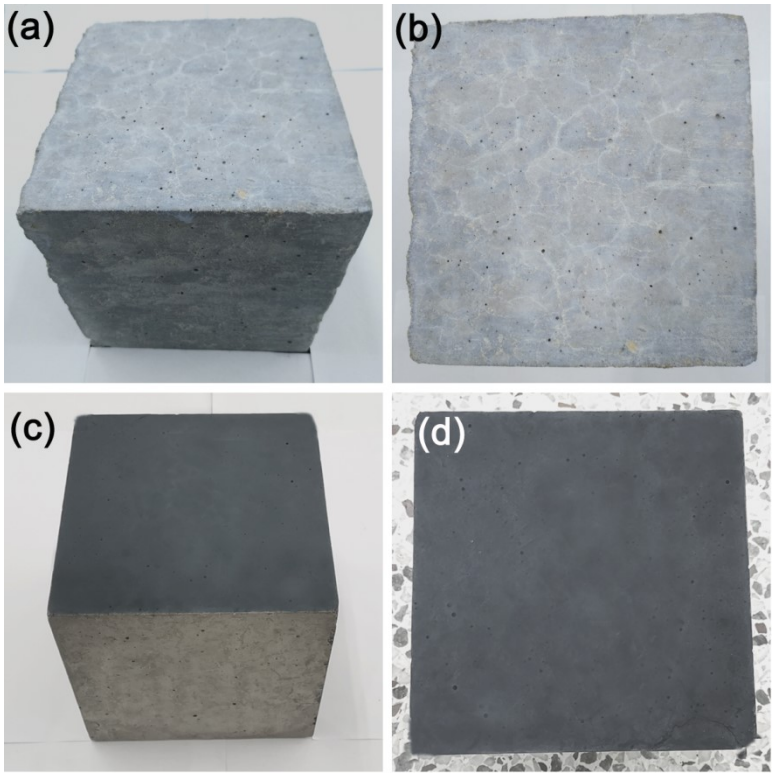

Fig. S9 Photographs of the Eco-blocks prepared without adding water-glass binder: (a) WCPE-20-w/o-B and its corresponding surface layer (b); and (c) BCPE-20-w/o-B and its corresponding surface layer (d).

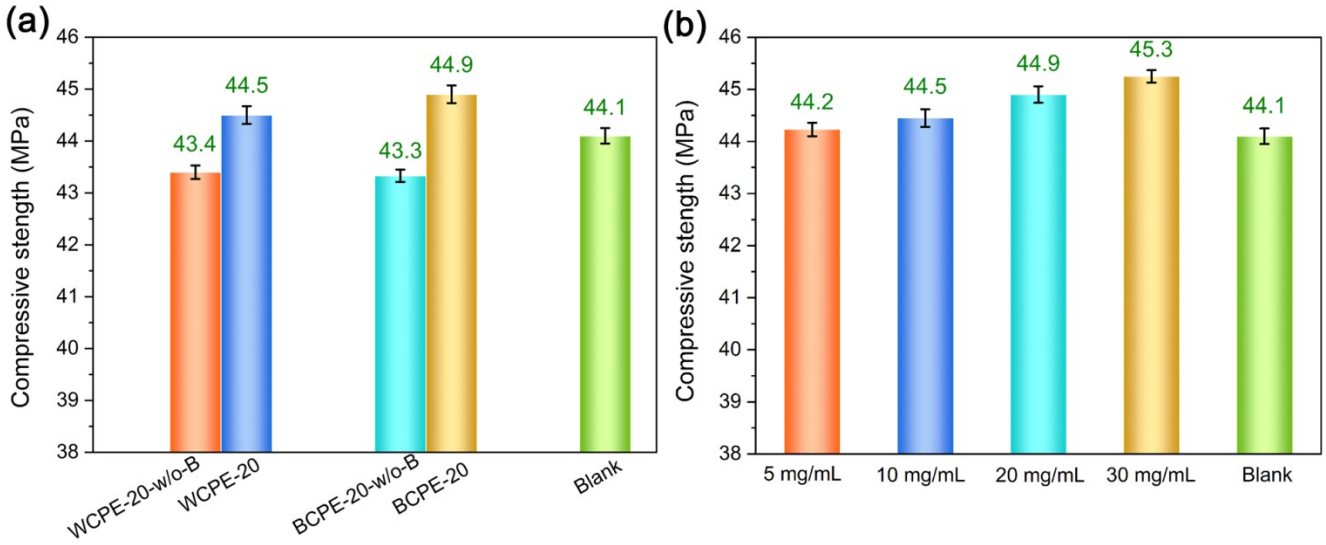

Fig. S10 (a) The effects of water-glass binder and (b) concentration of B-TiO_2 suspension on the compressive strength of as-prepared concrete paving Eco-blocks.

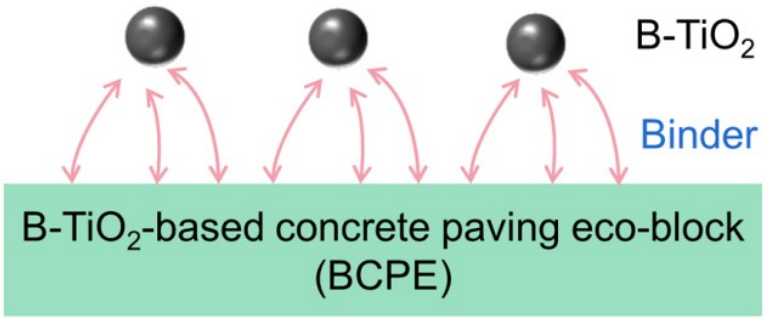

Scheme S3 Schematic illustration for the role of water-glass binder on the enhanced compressive strength.

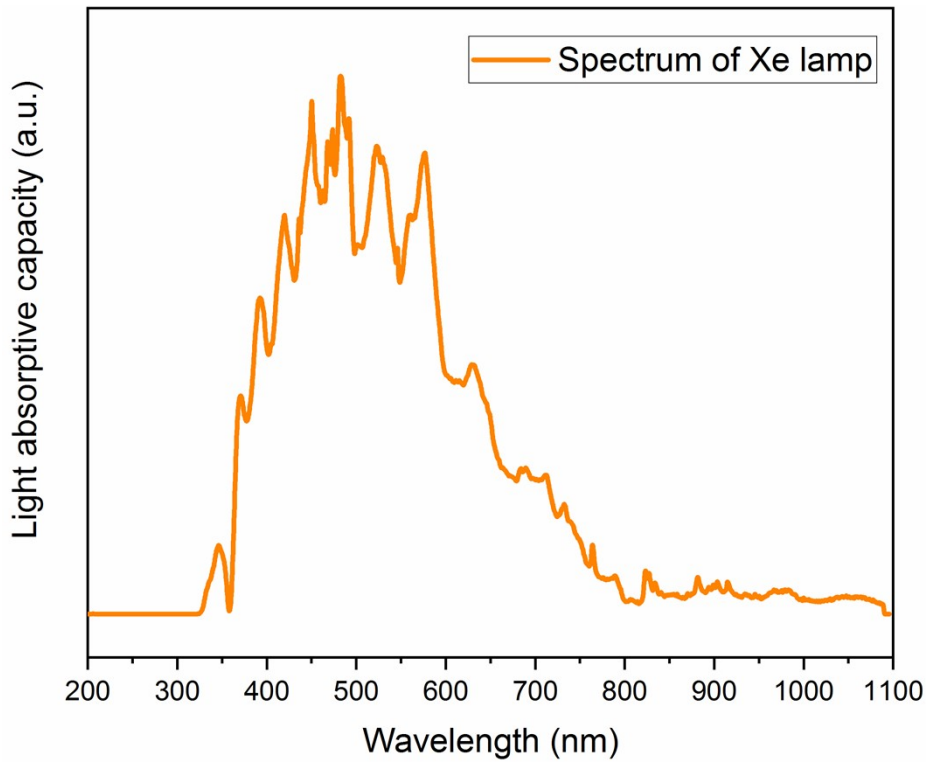

Fig. S11 The spectrum of Xe lamp (simulated solar light irradiation)

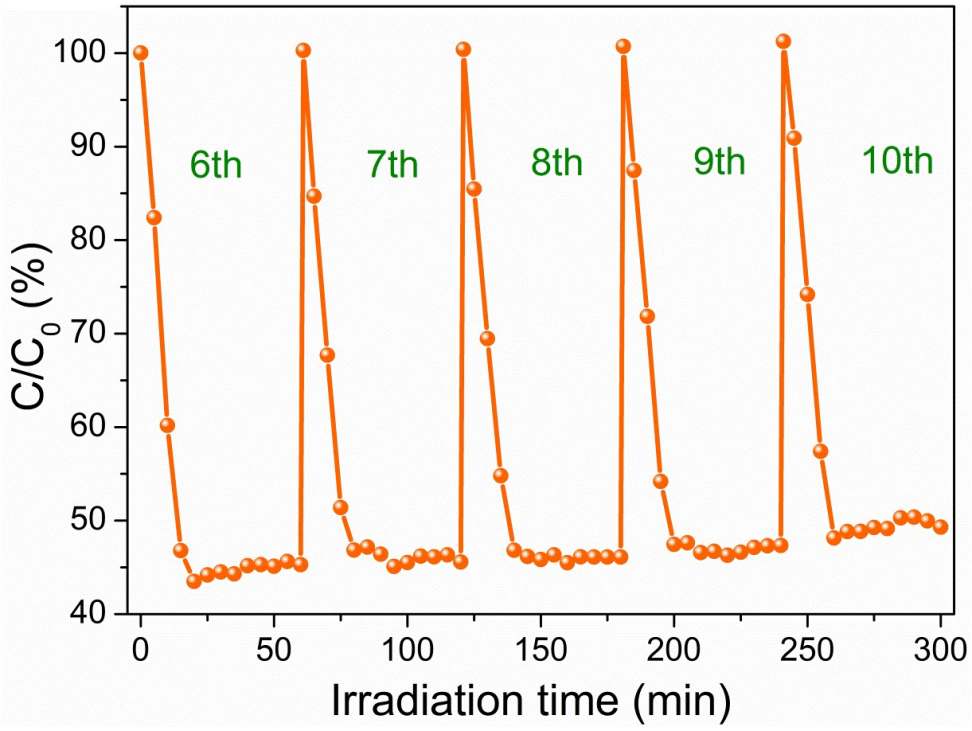

Fig. S12 Stability tests of BCPE-20 after washing with water.

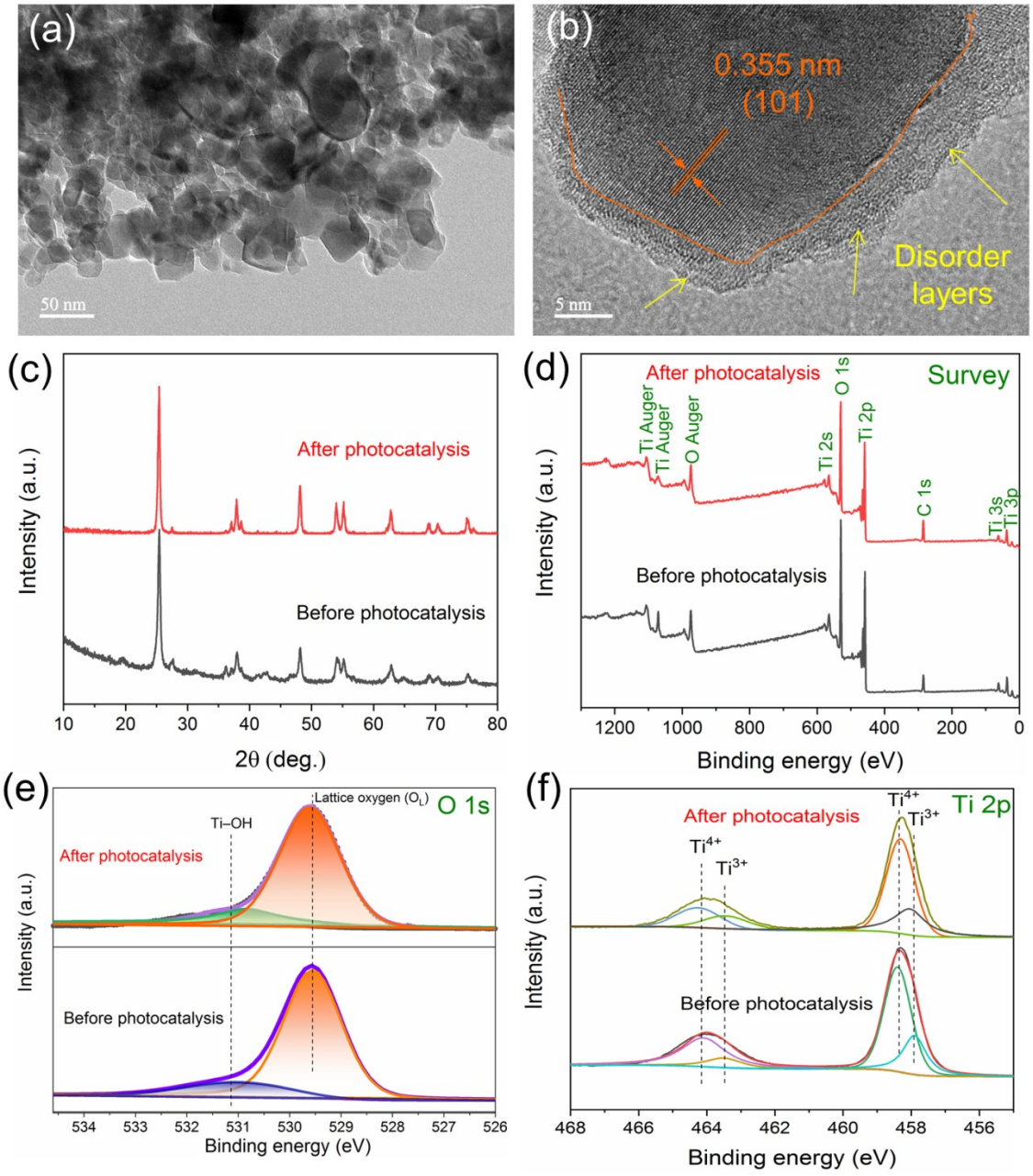

Fig. S13 (a) TEM and (b) HRTEM images of B-TiO_2 after photocatalysis. A comparison of (c) XRD patterns, (d) survey, (e) O 1s, and (d) Ti 2p high-resolution XPS spectra of B-TiO_2 before and after photocatalysis.

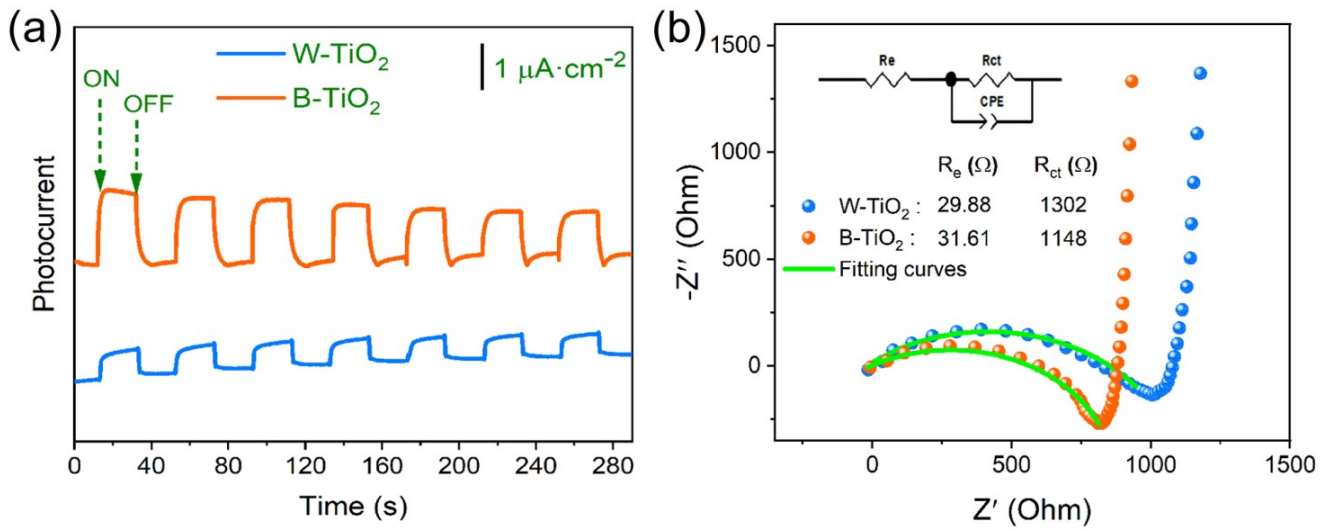

Fig. S14 (a) Photocurrent responses (I-t). (b) EIS Nyquist plots of various samples (inset shows the equivalent circuit model and the fitted results).

The EIS profiles are fitted through the equivalent circuit model (inset in Fig. S11b) using Zview software. The R_{ct} and R_s represent the charge transfer resistance and series resistance, respectively [3]. The fitting results demonstrate that B-TiO_2 reveals smaller R_{ct} compared to W-TiO_2, indicating a decreased charge interfacial transfer resistance of B-TiO_2.

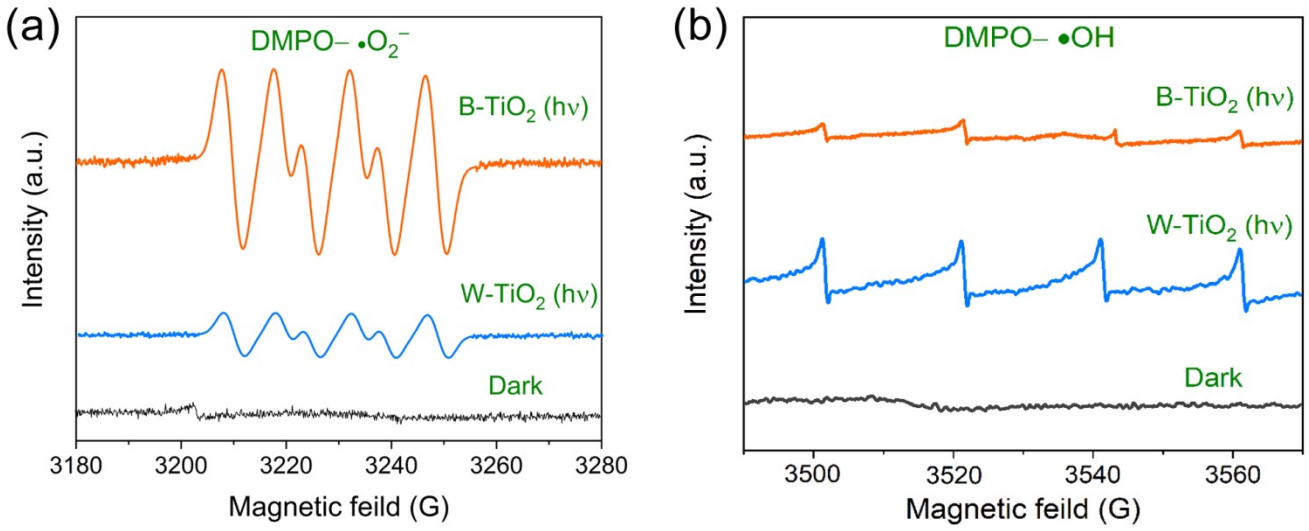

Fig. S15 DMPO spin-trapping EPR spectra of B-TiO_2 and W-TiO_2 for $\bullet O_2^-$ (a) and •OH (b) radicals under simulated solar light illumination.

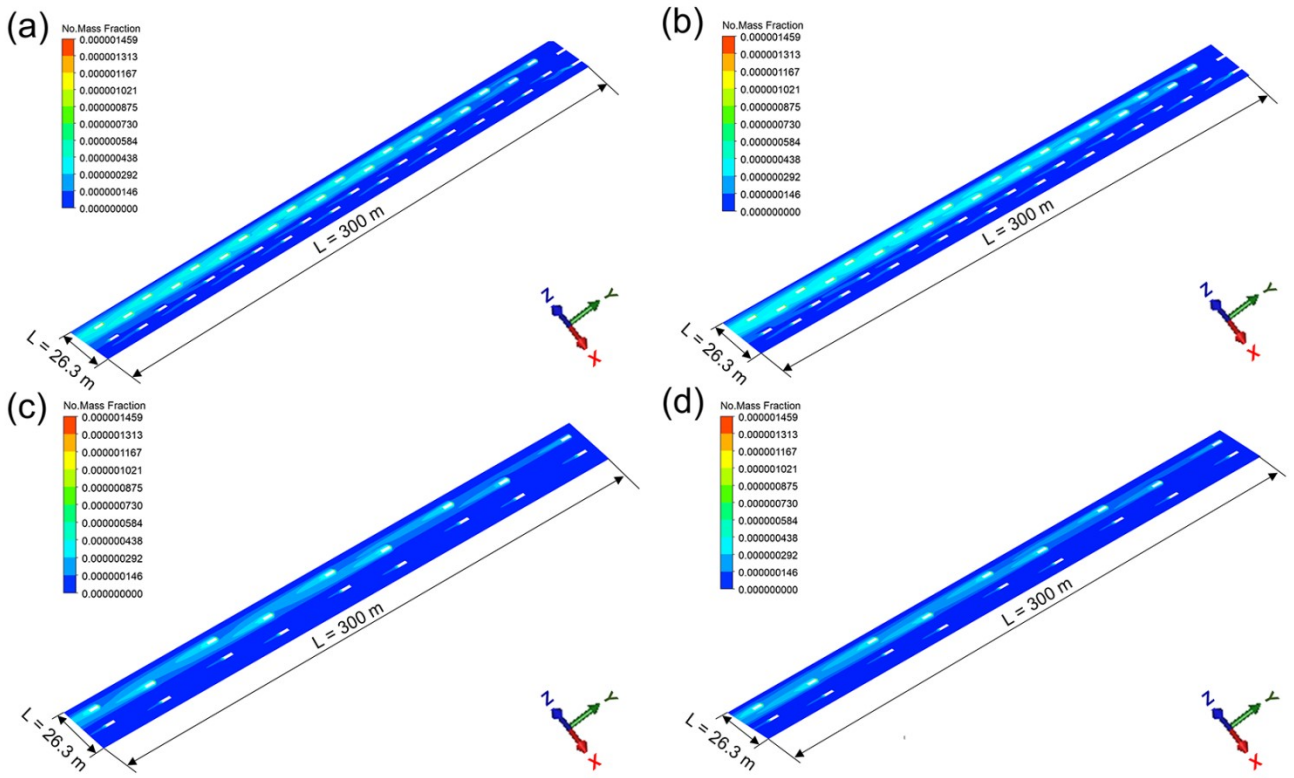

Fig. S16 CFD simulation of the concentration distribution of NO: (a) at the wind speed of 1 m s^{-1}, and (b) at the wind speed of 2 m s^{-1} with the vehicle speed of 10 km h^{-1}; (c) at the wind speed of 1 m s^{-1}, and (d) at the wind speed of 2 m s^{-1} with the vehicle speed of 60 km h^{-1}.

Table S1 The ambient air quality standard for NO_x (GB 3095-2012)

Pollutants	Average time	The limit value of NO_x concentration		Unit
		Level 1[a]	Level 2[b]	
NO_x	Annual average	50	50	μg m^{-3}
	24-hour average	100	100	
	1-hour average	250	250	

[a]represents the natural reserves, tourist attraction areas, and other areas requiring special protection;

[b]represents the residential areas, commercial traffic and residential mixed areas, cultural areas, industrial areas, and rural areas.

Table S2 The abrasion resistance of as-prepared concrete paving Eco-blocks.

Type	Blank control	BCPE-20	WCPE-20
Rotating revolutions of grinding wheel /r	4000	4000	4000
Grinding depth /mm	0.56	0.68	0.62
Abrasion resistance	3.57	2.94	3.23

Table S3 Summary of photocatalytic NO removal over various TiO_2-based concrete materials.

Photocatalyst	Building material	Preparation conditions	NOx purification efficiency	Ref.
Black TiO_2 (B-TiO_2)	Cement mortar	Spraying the B-TiO_2 suspension on the surface of the incompletely hardened concrete	Simulated solar light – NO (1 ppm): the highest removal ratio reaches 63.45% (at RH = 30%)	This work
Au/N–TiO_2/SiO_2	Limestone, granite, concrete	Spraying TiO_2/SiO_2 sols onto the surface of building materials	UV–Vis light – NO (1000 ppb) removal: 344 μmol/(m^2·h), 24.5%.	[4]
Pristine commercial TiO_2 (P25), Fe–TiO_2, V–TiO_2	Cement mortar	Mixing with cement mortar (0.5–2.5 wt%)	Solar light – NO (500 ppb) highest conversion rate: 15% TiO_2 (P25)	[5]
Pristine commercial TiO_2 (P25)	Cement mortar	Intermixed and spray-coated with nano-TiO_2	UV light – NO (1000 ppb): 60% removal ratio (5% spray-coated sample)	[6]
TiO_2–SiO_2	Cement mortar	Spraying the suspension of TiO_2 and SiO_2 sols	UV light – NOx (0.55 mg L^{-1}): 53% for NOx photodegradation	[7]
TiO_2 with a size of 35 nm	Cement mortar	Mixing with cement mortar (1, 3, 5, 10%)	UV light – NO (1 ppm): 36% NO removal rate (5 wt% TiO_2)	[8]
Supported TiO_2 (quartz sand)	Cement mortar	Surface-mounted TiO_2-aggregate	Solar simulator – NO (1000 ppb): 51.4% NO removal ratio	[9]
Pristine commercial TiO_2 (P25)	Cement mortar	Mixing with cement mortar (1 wt%)	UV light – NOx (1000 ppb): 25% removal efficiency	[10]

Photocatalyst	Building material	Preparation conditions	NOx purification efficiency	Ref.
Pristine commercial TiO_2 (P25)	Cement paste	Mixing with 10% TiO_2 replacement by mass of cement	UV light – NO (1000 ppb): 31% NO removal	[11]
Pristine commercial TiO_2 (P25)	Cement mortar	Mechanical mixer	UV light – NO (1000 ppb): 5.8% NOx removal ratio (2 wt% TiO_2)	[12]
Pristine commercial TiO_2	Cement mortar	Mixing with mortar (3, 5, and 10 wt%)	UV light – NO (1 ppmv) 36.9% removal rate	[13]
Ce-TiO_2	Asphalt mixture	Surface spraying method	Simulated solar light – NO (1.25 ppm): 27.38% NO removal efficiency	[14]
Pristine commercial TiO_2 (P25)	Cement mixed with recycled glass and/or sand (base)	Mixing with base (2–10 wt%)	UV light – NO (400 ppb) removal: 4 mg/(m^2·h); (1 wt% TiO_2)	[15]

Table S4 Assignments of the DRIFTS bands observed during NO adsorption and NO oxidation over B-TiO_2.

Wavenumber (cm^{-1})	Possible assignment	References
3784	Surface-free OH groups	16, 17
3642	H-bonded OH groups	16, 17
2920, 2858	NO_2	18, 19
1682	NO^+	18, 19
1588, 1448	Bidentate nitrates (NO_3^-)	20-23
1156, 1095	Nitrites (NO_2^-)	17, 20, 21, 24
962	N_2O_3	18, 21

References

1. H. Tan, Z. Zhao, M. Niu, C. Mao, D. Cao, D. Cheng, P. Feng and Z. Sun, *Nanoscale*, 2014, **6**, 10216-10223.
2. H. Zhang and J. F. Banfield, *J. Phys. Chem. B*, 2000, **104**, 3481-3487.
3. C. Zhang, D. Lei, C. Xie, X. Hang, C. He and H. L. Jiang, *Adv. Mater.*, 2021, **33**, e2106308.
4. M. Luna, J. M. Gatica, H. Vidal and M. J. Mosquera, *J. Clean. Prod.*, 2020, **243**, 118633.
5. M. Pérez-Nicolás, I. Navarro-Blasco, J. M. Fernández and J. I. Alvarez, *Constr. Build. Mater.*, 2017, **149**, 257-271.
6. M.-Z. Guo, T.-C. Ling and C. S. Poon, *Cem. Concr. Res.*, 2017, **83**, 279-289.
7. C. Mendoza, A. Valle, M. Castellote, A. Bahamonde and M. Faraldos, *Appl. Catal. B*, 2015, **178**, 155-164.
8. D. Seo and T. S. Yun, *Build. Environ.*, 2017, **112**, 233-240.
9. L. Yang, A. Hakki, L. Zheng, M. R. Jones, F. Wang and D. E. Macphee, *Cem. Concr. Res.*, 2019, **116**, 57-64.
10. R. Sugrañez, J. I. Álvarez, M. Cruz-Yusta, I. Mármol, J. Morales, J. Vila and L. Sánchez, *Build. Environ.*, 2013, **69**, 55-63.
11. B. Y. Lee, A. R. Jayapalan, M. H. Bergin and K. E. Kurtis, *Cem. Concr. Res.*, 2014, **60**, 30-36.
12. M.-Z. Guo, J. Chen, M. Xia, T. Wang and C. S. Poon, *Build. Environ.*, 2018, **144**, 412-418.
13. G. Hüsken, M. Hunger and H. J. H. Brouwers, *Build. Environ.*, 2009, **44**, 2463-2474.
14. X. Cao, X. Yang, H. Li, W. Huang and X. Liu, *Constr. Build. Mater.*, 2017, **148**, 824-832.
15. C. S. Poon and E. Cheung, *Constr. Build. Mater.*, 2007, **21**, 1746-1753.

16. T. H. Lim, S. M. Jeong, S. D. Kim and J. Gyenis, *J. Photochem. Photobiol. A: Chem.*, 2000, **134**, 209-217.

17. J. C. S. Wu and Y.-T. Cheng, *J. Catal.*, 2006, **237**, 393-404.

18. J. Laane and J. R. Ohlsen, in *Prog. Inorg. Chem.*, 1980, DOI: https://doi.org/10.1002/9780470166284.ch6, pp. 465-513.

19. M. Ran, H. Wang, W. Cui, J. Li, P. Chen, Y. Sun, J. Sheng, Y. Zhou, Y. Zhang and F. Dong, *ACS Appl. Mater. Interfaces*, 2019, **11**, 47984-47991.

20. K. I. Hadjiivanov, *Catal. Rev.*, 2000, **42**, 71-144.

21. H. Wang, Y. Sun, G. Jiang, Y. Zhang, H. Huang, Z. Wu, S. C. Lee and F. Dong, *Environ. Sci. Technol.*, 2018, **52**, 1479-1487.

22. G. Ramis, G. Busca, V. Lorenzelli and P. Forzatti, *Appl. Catal.*, 1990, **64**, 243-257.

23. K. Hadjiivanov, V. Bushev, M. Kantcheva and D. Klissurski, *Langmuir*, 1994, **10**, 464-471.

24. N. Isao, S. Shinichi and T. Koji, *Chem. Lett.*, 2000, **29**, 1276-1277.